

## Article

# A Systematic Investigation of Lead-Free Electroless Ni-B-W Coating Properties Using Taguchi's Methodology

Rohit Agrawal, Om Prakash, Lakhbir Singh Brar  and Arkadeb Mukhopadhyay \* 

Department of Mechanical Engineering, Birla Institute of Technology, Mesra, Ranchi 835215, India; phdme10004.20@bitmesra.ac.in (R.A.); omprakash@bitmesra.ac.in (O.P.); brarls@bitmesra.ac.in (L.S.B.)

\* Correspondence: arkadeb.mukhopadhyay@bitmesra.ac.in

**Abstract:** Electroless Ni-B (ENB) coatings have industrial importance due to their excellent mechanical properties. The inclusion of W (ENB-W) to the coatings further enhances their mechanical properties and thermal stability. Nevertheless, the ENB or ENB-W coatings are deposited from a heavy metal-stabilized bath, and the very commonly used stabilizer is lead nitrate. The present work is an attempt to obtain an ENB-W coating with enhanced mechanical properties and elimination of the stabilizer from the bath. To achieve this, the coating bath temperature, the heat treatment temperature and the heat treatment duration were varied systematically following a strategy adopted from Taguchi's experimental design. The mechanical properties targeted include surface microhardness and scratch hardness. Multi-objective optimization was performed using gray relational methodology. The predicted bath temperature was 85 °C, while the predicted heat treatment temperature was 450 °C and there was 3 h of heat treatment time. The optimized lead-free ENB-W coatings had a microhardness of 1096.2 HV<sub>100</sub> and scratch hardness of 13.86 GPa. In fact, single-objective optimization for surface microhardness and scratch hardness by Taguchi's methodology also predicted the same optimal parametric condition for both scratch hardness and surface microhardness. This was comparable to that of a lead-stabilized ENB-W coating and higher than the as-plated stabilizer free ENB-W coatings. The coating failure of the optimized ENB-W alloy was tested using a progressive scratch test, which showed that there was no chevron or transverse cracks within the load range considered. Analysis of corrosion resistance revealed that the corrosion potential of the optimized coatings was −407 mV, and this was comparable to that of a lead-based ENB-W coating.

**Keywords:** electroless Ni-B-W; heat treatment; microhardness; scratch hardness; gray relational analysis; corrosion resistance



**Citation:** Agrawal, R.; Prakash, O.; Brar, L.S.; Mukhopadhyay, A. A Systematic Investigation of Lead-Free Electroless Ni-B-W Coating Properties Using Taguchi's Methodology. *Coatings* **2023**, *13*, 1585. <https://doi.org/10.3390/coatings13091585>

Academic Editor: Yiping Guo

Received: 12 July 2023

Revised: 3 September 2023

Accepted: 5 September 2023

Published: 11 September 2023



**Copyright:** © 2023 by the authors. Licensee MDPI, Basel, Switzerland. This article is an open access article distributed under the terms and conditions of the Creative Commons Attribution (CC BY) license (<https://creativecommons.org/licenses/by/4.0/>).

## 1. Introduction

The deposition of nickel-based coatings with useful mechanical properties and tribological characteristics can be completed by an electroless method [1]. The coatings have commendable hardness, wear resistance and corrosion resistance [2]. The usefulness of this method lies in the fact that complex geometry can be coated with ease [3]. The coating formulation consists of different chemicals that act as sources of Ni, reducing agents, complexing agents, buffers, surfactants, etc. [2,3]. Any complex part when immersed into the bath receives homogenous deposition in terms of its thickness [3]. Primarily, Ni-P (ENP) and Ni-B (ENB) coatings can be deposited by this method depending on the reducing agent chosen [3]. With further research and development and increasing needs from industries, the nickel-based coatings have developed into a wider family with multiple poly-alloy and nanocomposites with superior mechanical properties [2,3]. Therefore, the coatings have gained popularity in automotive, aerospace, defense, printing, textile, and electronic applications [1].

Amongst the ENP and ENB, the latter has gained popularity due to its wear protection capabilities. Enhancement in their properties could be achieved by the addition of tungsten

(W) to the matrix of ENB, which includes hardness, wear and corrosion resistance, frictional behavior, thermal and electrochemical properties and leads to the deposition of Ni-B-W (ENB-W) coatings [4–7]. There was a significant increase in the as-deposited hardness of the ENB-W coating compared to binary ENB [4]. In fact, high-temperature tribological tests also revealed that oxides of tungsten can have a self-lubricating effect at the sliding interface [5]. Drovosekov et al. [7] investigated an ENB-W coating with varying W content, and it was found that W inclusion could influence the crystallization temperature of the coatings, leading to higher thermal stability. The enhanced tribological behavior at high temperature was attributed to this by Mukhopadhyay et al. [8]. It was seen that the coatings performed well at 300 and 500 °C due to the increased thermal stability. Furthermore, TGA analysis revealed a higher thermal stability of ENB-W compared to ENB obtained from a stabilizer-free bath [9]. Another key finding that enhances the superior properties of ENB-W coatings is the oxidation resistance [10]. High-temperature oxidation studies revealed that an interdiffusion of Fe from the substrate can be restricted by the inclusion of W.

Mostly, the ENB-W coatings were deposited by varying sodium tungstate in a coating bath within the range 15–35 g/L [5,8,9,11–14]. The W exists in coatings in solid solution form and results in solid solution strengthening of the coating matrix. This further enhances the mechanical properties and tribo-performance compared to ENB. Within this range, the coatings appear either nodular or as aggregates of nodules resembling the surface of a cauliflower [11,12]. The cross-section appears to have columnar growths for the lead nitrate-stabilized ENB-W coatings which reduces the actual contact area and prevents adhesion [11], resulting in enhanced performance. Apart from solid solution strengthening, the coating matrix can be also toughened by heat treatment within the range 350–650 °C [8,12–16]. Heat treatment promotes the crystallization of the ENB-W coating matrix by inducing structural transformations. This leads to marked improvement in both the hardness and wear resistance of the coating [4,5,8]. Post-heat treatment, hard boride phases are precipitated [13–16]. In fact, heat-treated ENB-W coatings were suggested to have better corrosion resistance [6]. Apart from surface microhardness, wear and corrosion resistance, the mechanical properties of ENB-W coatings can be also characterized by performing scratch tests, which gives useful information about scratch hardness, critical load of failure and fracture toughness [13–15,17,18]. The scratch hardness of the ENB-W coating was found to be 6.68 GPa while the fracture toughness was 3.66–3.98 MPa m<sup>0.5</sup> [15]. The properties increase by the addition of SiC in the coating matrix, which resulted in dispersion strengthening [14,17]. In fact, Zhao et al. [16] reported an increase of 8.9% in the fracture toughness of ENB-W compared to ENB. The scratch hardness of ENB-W coatings obtained from a lead-free bath were also found to be higher than that of the binary ENB alloy obtained at similar conditions [9,18].

Doubtlessly, ENB-W ternary coatings have emerged as potent options for protective purposes in several mechanical and tribological applications. But the ENB or ENB-W coatings are developed from a heavy metal/lead nitrate/lead tungstate-stabilized bath [1,13–16]. Therefore, there is a need to eliminate such toxic elements from the electroless bath looking into the future and sustainability of the coatings [1]. In some recent studies, an optimized ENB coating could be deposited from a stabilizer-free bath [19], and they presented comparable properties with the lead-stabilized counterparts [20]. Similar results were also reported for an as-deposited ENB-W coating obtained from a stabilizer-free bath by Agrawal and Mukhopadhyay [9]. Thus, ENB-W coatings obtained from a stabilizer-free bath should be explored further. As per the present scenario, the heat treatment of ENB-W coatings (stabilizer-free bath) remains uninvestigated. Therefore, the present work is directed toward the same, and a systematic study with the help of design of experiments and statistical techniques is attempted. The coating bath temperature was varied between 85 and 95 °C, since prior work suggests that an ENB-W coating with varying W and B content can be deposited [9]. Furthermore, the heat treatment temperature and duration varied in the ranges of 350–450 °C and 1–3 h, respectively. The effects of this on the

surface microhardness and scratch tests were investigated. Single-objective optimization was performed with the help of Taguchi's analysis. The scratch hardness and surface microhardness were simultaneously optimized. A simplistic gray relational analysis (GRA) approach was undertaken. Analysis of variance (ANOVA) was conducted to study the statistical influence of the experimental parameters. The morphological changes were detected using a field-emission scanning electron microscope (FESEM). Poor adhesion of the ENB-W coatings (lead stabilizer free) was reported in a recent study [9]. Thus, in a quest to determine first the critical load of failure, a progressive scratch test on an optimized coating was also performed. Finally, the corrosion resistance of optimized coatings was examined using an electrochemical method, and the corrosion mechanism was analyzed in detail.

## 2. Materials and Methods

On medium carbon steel samples (AISI 1040), electroless depositions were performed ( $15 \times 15 \times 2 \text{ mm}^3$ ). The substrates were thoroughly cleaned prior to deposition. AISI 1040 steel specimens were immersed in acetone and then rinsed with deionized water. Then, specimens were dipped in sulfuric acid to remove oxide and rust and to form active sites on the surface. The samples were rinsed with deionized water and were ready for the coating bath process. All these processes were carried out sequentially. To achieve an even dispersion of constituents throughout the deposition process, a magnetic stirrer was utilized. Table 1 shows the chemical constituents and operational parameters of a bath [9]. After deposition, samples were removed from the bath, cleaned with deionized water, and dried. FESEM was used to visualize the coating surface (Sigma 300, Carl Zeiss, Germany). Using X-ray diffraction (XRD) with Cu-K $\alpha$ , a step size of  $0.02^\circ$  and a scan rate of  $5^\circ/\text{min}$  for  $2\theta$  ranging between 20 and  $80^\circ$ , phase and structural analyses of coatings were carried out (Smart Lab, Rigaku, Japan). Then, they were subjected to heat treatment in a muffle furnace as per the scheme tabulated in Table 2.

**Table 1.** Chemical composition of bath of ENB-W coatings.

Parameter Used for Deposition	Amount (g/L)	Functions of Chemicals
Nickel chloride	25	Source of nickel
Sodium hydroxide	40	Buffering agent
Ethylene diamine	55	Complexing agent
Sodium borohydride	0.8	Reducing agent
Sodium tungstate	25	Source of tungsten
Deposition temperature	$(85, 90, 95) \pm 2^\circ\text{C}$	-
Deposition duration	2 h	-

**Table 2.** Process parameters, their levels and symbols denoting process parameters.

Level	Bath Temperature ( $^\circ\text{C}$ ) Denoted by Symbol 'A'	Heat Treatment Temperature ( $^\circ\text{C}$ ) Denoted by Symbol 'B'	Duration of Heat Treatment (Hours) Denoted by Symbol 'C'
1	85 (A <sub>1</sub> )	350 (B <sub>1</sub> )	1 (C <sub>1</sub> )
2	90 (A <sub>2</sub> )	400 (B <sub>2</sub> )	2 (C <sub>1</sub> )
3	95 (A <sub>3</sub> )	450 (B <sub>3</sub> )	3 (C <sub>1</sub> )

The process parameters and their levels are tabulated in Table 2. They are the coating bath temperature, heat treatment temperature and heat treatment duration. To minimize the number of trials, Taguchi's L<sub>9</sub> orthogonal array (OA) was employed as an experimental design. Taguchi's L<sub>9</sub> OA is based on the OA prescribed by Taguchi for experimental design. In the L<sub>9</sub> OA, a total of nine experiments are to be carried out. The selection of the OA is based on degrees of freedom. Since three factors are considered at three equally spaced levels (without interaction effects), the degrees of freedom is 6. Hence, L<sub>9</sub> OA is selected,

which can accommodate eight degrees of freedom. Several coated specimens were heat treated at 350, 400 and 450 °C for 1, 2 and 3 h in a muffle furnace in the presence of air in accordance with L<sub>9</sub> OA. After this, coatings were evaluated for their mechanical and microstructural characteristics. Figure 1 shows a comprehensive flowchart of the testing and characterization of coatings.

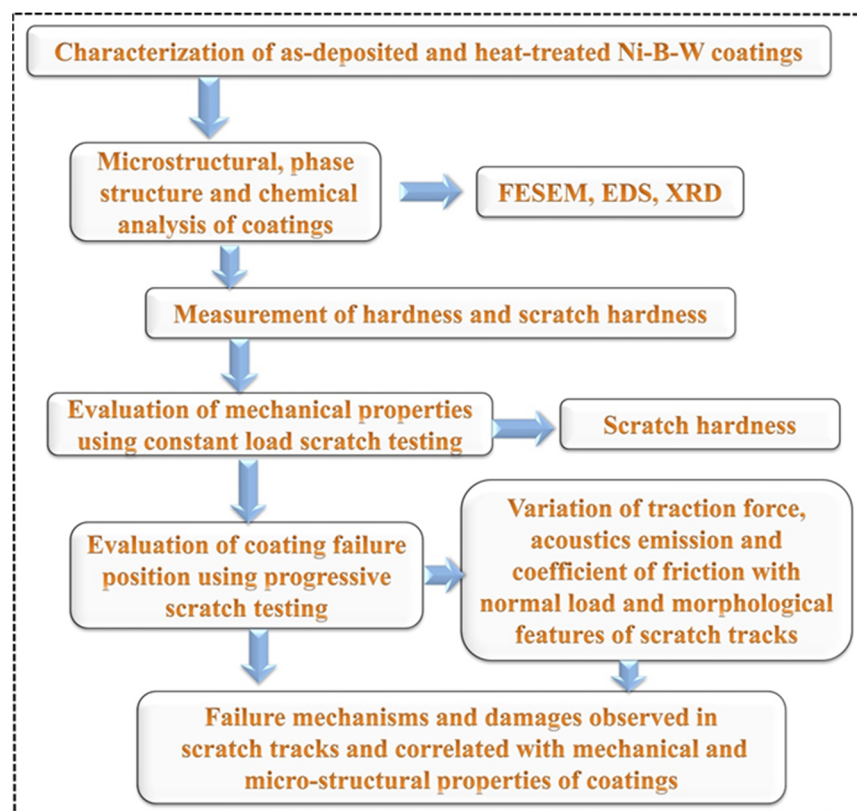


**Figure 1.** Schematic of work flow.

Hardness tests were performed with a microhardness tester using a Vickers indenter at a 100 gf load and 15 s of holding time (VHS1000A1, Banbros Engineering, Delhi, India). The surface microhardness was determined by taking the average of five readings at different positions on the surface. All scratch tests were executed using a scratch tester fitted with a Rockwell C diamond indenter (apex angle: 120°, tip radius: 200 µm, Unitest 250, Ducom Instruments, Bengaluru, India). The surface of each coating was subjected to a constant load of 10 N to determine the scratch hardness. The scratch hardness was determined from three scratches with 10 readings of width taken from each scratch. After optimization, progressive scratch tests were completed to evaluate first critical load of coating failure, which was performed over a 10 mm stroke length and 1 N/s loading rate within the range of 5–24 N. The speed of the indenter was 0.5250 mm/s. An examination of morphological features and structure was completed for optimized coatings using FESEM and XRD, respectively. The scratched surface and damage were visualized using FESEM to obtain a deeper insight.

By using potentiodynamic polarization (PDP) electrochemical test methods, the corrosion of ENB-W coatings was examined (680B, CH Instruments, Austin, TX, USA). The corrosion resistance performance was in a corrosive media containing 3.5 wt.% NaCl solution. The samples were exposed to a surface area of 1 cm<sup>2</sup>. The potential difference was measured using a reference electrode. The applied current was made to flow to solution through an auxiliary electrode. Working electrodes were ENB-W coated specimens, whereas auxiliary electrodes and reference electrodes were platinum wire and silver chloride, respectively. The potential was varied in the range of 0 to 1.2 V/SCE at a scan rate

of  $0.01 \text{ Vs}^{-1}$ . From the Tafel plot, the corrosion potential ( $E_{\text{corr}}$ ) was estimated. Finally, FESEM and EDS mapping were used to examine corrosion mechanisms.

### 2.1. Taguchi's Method for Single-Objective Optimization

Genichi Taguchi was one who first proposed this method [21]. To achieve good quality at a reasonable price, Taguchi's method is used in this work to identify the best parametric combination for maximizing hardness and scratch hardness. Microhardness and scratch hardness were used as a response to investigate the signal to noise ( $S/N$ ) ratio. For microhardness and scratch hardness, higher-the-better (HB) criteria were used. The  $S/N$  ratio (dB) was determined as:

$$S/N = -10 \log\left(\frac{1}{n} \sum \frac{1}{y^2}\right) \quad (1)$$

where  $n$  is the number of observations and  $y$  is the observed data.

The statistical significance of each factor was evaluated using ANOVA. At the end, a verification test was performed using a combination of process parameters that results in an optimal condition. The predicted  $S/N$  ratio is determined as:

$$\hat{n} = n_m + \sum_{i=1}^o (n_i - n_m) \quad (2)$$

where  $\hat{n}$  is the predicted  $S/N$  ratio,  $n_m$  is the mean  $S/N$  ratio,  $n_i$  is the mean  $S/N$  ratio at an optimal level and ' $o$ ' is the number of process parameters. The predicted  $S/N$  ratio and experimentally obtained value should be in proximity. Furthermore, a comparison is also carried out with any arbitrary condition which is denoted as an initial test condition. In general, a mid-level combination is considered as the initial test condition.

### 2.2. GRA

Deng introduced GRA, an outstanding tool that effectively handles uncertain and multi-variate systems [22]. White signifies complete information while black signifies no information. GRA deals with information that is gray. The responses are transformed into a single multi-performance index as gray relational grade (GRG) [23]. The GRG is used to conduct additional analysis and optimization. The GRA algorithm is described as follows:

Step 1. Gray relational generation, where a set of experimental outcomes are normalized in the range of 0 and 1. Hardness and scratch hardness should be maximized, so HB criteria were used as follows:

$$x_i^*(k) = \frac{y_i(k) - \min y_i(k)}{\max y_i(k) - \min y_i(k)} \quad (3)$$

where  $\max y_i(k)$  is the largest of  $y_i(k)$  and  $\min y_i(k)$  is the lowest of  $y_i(k)$ .

Step 2. Using normalized data, gray relational coefficients (GRC) are computed.

GRC ( $\zeta_i(k)$ ) may be determined as:

$$\zeta_i(k) = \frac{\Delta_{\min} + r\Delta_{\max}}{\Delta_{0i}(k) + r\Delta_{\max}} \quad (4)$$

where  $\Delta_{0i} = ||x_{0i}(k) - x_i^*(k)||$  = difference of absolute value among  $x_{0i}(k)$  and  $x_i^*(k)$ ,  $\Delta_{\min}$  and  $\Delta_{\max}$  are the minimum and maximum values of absolute differences  $\Delta_{0i}$ , respectively,  $r$  is a distinguishing coefficient and  $r \in \{0, 1\}$ . In this work,  $r = 0.5$  is taken because of the good stability of outcomes.

Step 3. GRG is evaluated by averaging the GRC. Instead of multiple responses of hardness and scratch hardness, GRG is taken as an overall response of the process

$$\gamma_i = \frac{1}{n} \sum_{k=1}^n \xi_i(k) \quad (5)$$

where  $n$  is the number of performance characteristics.

Step 4. Using GRG and statistical ANOVA, identify an input parameter that has a substantial impact on the performance of the process.

Step 5. Choose the best/optimal process parameter combination.

Step 6. Perform confirmation experiments to validate the best/optimal process configuration.

### 3. Results and Discussion

#### 3.1. Characterization of ENB-W Coatings before Heat Treatment

The surface morphology of ENB-W coatings before heat treatment formed at  $A_1$ ,  $A_2$ , and  $A_3$  has a densely packed nodulated morphology as depicted in Figure 2a–c, respectively [4,6,7,10,15,16]. However, higher magnification images reveal a cauliflower-like surface, which has been reported by Agrawal and Mukhopadhyay [9] for ENB-W coatings, and in the present case, they appear to be more of nodulated structures or like spherulites [24]. When the nodules form aggregates, then such a morphology has been commonly referred to as cauliflower-like morphology in ENB and ENB-W coatings, which is observed for both as-deposited and heat-treated coatings [11,25–30]. As the bath temperature increases, the nodules size also increases. These kinds of structures work well as lubricant retainers. Nodulated structures serve as rigid greasers, which reduce the abrasive impact of coatings [31,32]. The surface appears to be smooth, compact and uniform in the present work compared to that of a lead-stabilized ENB-W coating and is quite similar to the ENB coating obtained from the stabilizer-free bath. For stabilizer-free ENB coatings, Bonin et al. [19] found a similarly dense coating morphology. Stabilizers restrict the directed columnar growth of coatings that would result in a dense structure. However, as stated by Agrawal and Mukhopadhyay [9], the surface looked to be rough in comparison to lead-stabilized baths due to intense reactions taking place because of the absence of a stabilizer. Composition analysis revealed 3.25%, 1.70%, and 1.45% B as well as 1.65%, 2.10% and 2.45% W [9]. An average cross-sectional thickness of  $21.36 \pm 2 \mu\text{m}$ ,  $14.88 \pm 3 \mu\text{m}$  and  $14.68 \pm 2 \mu\text{m}$  for coatings deposited at  $A_1$ ,  $A_2$  and  $A_3$ , respectively, is obtained [9].

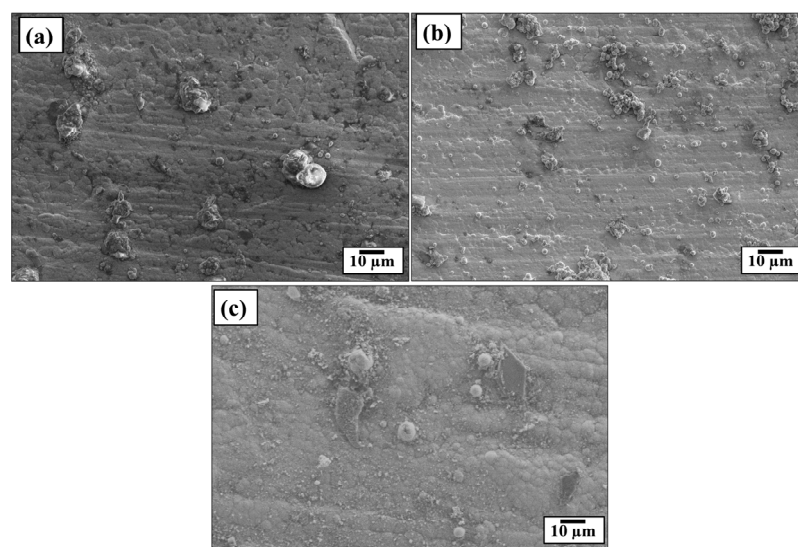


**Figure 2.** FESEM micrograph of as-deposited ENB-W deposited at (a)  $A_1$ , (b)  $A_2$ , and (c)  $A_3$ .

The XRD-based structural study of an ENB-W coating in its as-deposited states is depicted in Figure 3, which indicates its mixed amorphous and nanocrystalline nature. A sharp peak at  $44.9^\circ$  can be seen in XRD data which pertains to that of the coat-

ing overlapping with the substrate, and a similar behavior has been also detected by Vitry et al. [30]. An amorphous structure is usually observed in coatings with boron levels of 5 to 6 wt.% [27,33,34]. In ENB and ENB-W coatings with 5% B, amorphous and nanocrystalline structures coexist [15,18]. Similar results have been reported for a coating comprising 5.37 wt.% B by Balaraju et al. [35]. An amorphous phase is promoted by the inclusion of W [7]. Due to lower coating thickness, particularly at A<sub>2</sub>, peaks of Fe and Ni overlap with each other. Thus, this kind of behavior was also observed in ENB [18] as well as ENB-W [9] coatings deposited without stabilizers. The peak of Fe was from the substrate and has a resemblance with that seen in prior research studies where ENB was deposited on magnesium alloys [36]. It may be noted here that in this case, the crystallite size was not determined since the peaks of the substrate and Ni (111) coincide with each other.

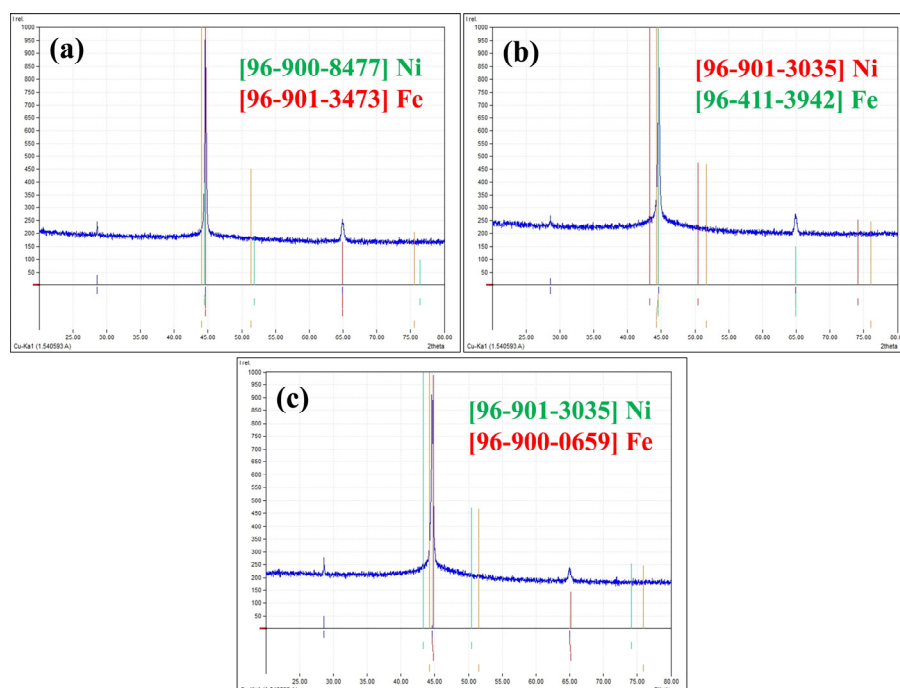


**Figure 3.** XRD analysis of as-deposited ENB-W deposited at (a) A<sub>1</sub>, (b) A<sub>2</sub>, and (c) A<sub>3</sub>. The coloured line (red and green) corresponds to Ni and Fe and has been given in the legend.

### 3.2. Surface and Contour Plot of Hardness and Scratch Hardness

Three-dimensional surface plots of microhardness with varying process parameters are shown in Figure 4. The plots are obtained based on the experimental data (Table 3). The corresponding contour plots are presented in Figure S1. For bath temperature and heat treatment temperature, higher hardness is observed at low levels of bath temperature and high levels of heat treatment temperature (Figure 4a). Again, in the interaction of heat treatment temperature and duration, maximum hardness is observed at high levels of both in Figure 4b owing to an increase in the degree of crystallinity and precipitation of hard boride phases. With the decrease in heat treatment temperature as well as time, the hardness decreases. Maximum hardness is detected at a low level of bath temperature and high level of heat treatment time in Figure 4c. Agrawal and Mukhopadhyay [9] observed that with the rise in bath temperature, the B content decreases and W content increases, resulting in a rise in microhardness. At a low level of bath temperature, the B content is 3.25 wt.% and W content is 1.65 wt.%. This may be considered to be in the low-B range. Also, the inclusion of W improves the thermal stability and shifts the temperature at which the crystallization of coatings take place [7,8]. Therefore, at the aforesaid composition, the highest heat treatment temperature and duration results in the crystallization of coatings and optimal crystallite size, which promotes the mechanical properties and prevents crack propagation (generally happens when grain coarsening takes place).

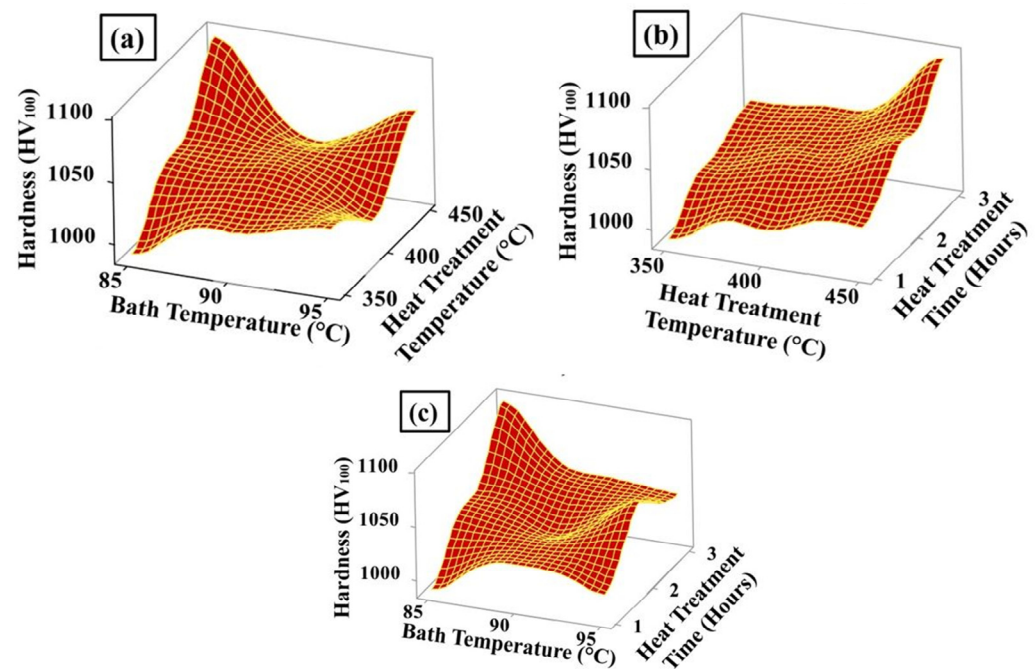


**Figure 4.** Three-dimensional (3D) surface plots of surface microhardness with variation of (a) heat treatment temperature vs. bath temperature, (b) heat treatment time vs. heat treatment temperature and (c) heat treatment time vs. bath temperature.

**Table 3.** Experimental results of Taguchi's *S/N* ratios, scratch hardness and surface microhardness, obtained in  $L_9$  OA.

Exp. No.	Hardness (HV <sub>100</sub> )	<i>S/N</i> Ratio of Hardness (dB)	Order	Scratch Hardness (GPa)	<i>S/N</i> Ratio of Scratch Hardness (dB)	Order
1	990	59.9127	9	11.64	21.3191	9
2	1036.95	60.3152	4	12.3	21.7981	4
3	1096.2	60.7978	1	13.86	22.8353	1
4	1020	60.1720	7	11.82	21.4523	7
5	1040.86	60.3478	3	12.38	21.8544	3
6	1025	60.2145	6	12.14	21.6844	6
7	1035.92	60.3065	5	12.28	21.7840	5
8	1010	60.0864	8	11.8	21.4376	8
9	1062.4	60.5258	2	12.68	22.0624	2

The 3D surface and contour plots based on the values given in Table 3 for scratch hardness are depicted in Figure 5 and Figure S2, respectively. For the interaction of bath and heat treatment temperature, at the lowest value of bath temperature and highest heat treatment temperature, the maximum scratch hardness is observed in Figure 5a. The minimum scratch hardness is noticed at the lowest bath temperature and lowest heat treatment temperature. Again, maximum scratch hardness is observed at the interaction of highest heat treatment temperature and highest heat treatment time in Figure 5b. On the other hand, minimum scratch hardness is observed at the lowest heat treatment temperature and lowest heat treatment time. Lastly, at the lowest bath temperature and highest heat treatment time, the maximum scratch hardness is observed in Figure 5c. Thus, the surface microhardness and scratch hardness have similar trends, and the same phenomenon occurs in both the cases.

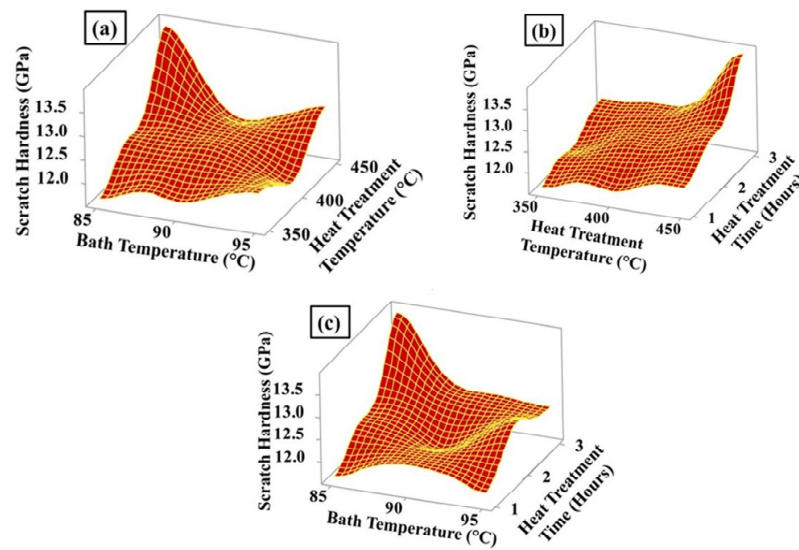


**Figure 5.** Three-dimensional (3D) surface plots of scratch hardness with variation of (a) heat treatment temperature vs. bath temperature (b) heat treatment time vs. heat treatment temperature and (c) heat treatment time vs. bath temperature.

3.3. Single-Objective Optimization of Hardness and Scratch Hardness

The *S/N* ratios for hardness and scratch hardness calculated by Equation (1) are presented in Table 3. The experimental design is OA, and hence, it is feasible to estimate the average impact of each design parameter on response at various levels. Hence, it is favorable to increase the microhardness and scratch hardness of coatings; both responses in this case were taken into consideration using the HB criteria listed in Equation (1). The mean *S/N* ratios for hardness and scratch hardness for each of the levels A, B, and C are presented in Table 4. It is called the response table. The delta values are obtained by deducting the lowest value from the highest value within the same column. According to Table 4, C is given rank 1, indicating that the heat treatment duration has the highest impact on hardness and scratch hardness. The values in Table 4 were used to generate the main effects plot, which is depicted in Figure S3. Figure S3 demonstrates that an ideal/optimal parameter combination is  $A_1B_3C_3$ .

**Table 4.** Response table for mean of *S/N* ratios of microhardness and scratch hardness of the ENB-W coatings.

Microhardness			
Level	A	B	C
1	60.34	60.13	60.07
2	60.24	60.25	60.34
3	60.31	60.51	60.48
Delta	0.1	0.38	0.41
Rank	3	2	1
Total mean of <i>S/N</i> ratio = 60.30 (dB)			
Scratch Hardness			
Level	A	B	C
1	21.98	21.52	21.48
2	21.66	21.7	21.77
3	21.76	22.19	22.16
Delta	0.32	0.68	0.68
Rank	3	2	1
Total mean of <i>S/N</i> ratio = 21.80 (dB)			

The results of ANOVA for hardness and scratch hardness are given in Table 5. It can be shown that the heat treatment time (C) has the greatest impact for hardness, which is followed by the heat treatment temperature (B) and the bath temperature (A), while the heat treatment temperature (B) has greatest impact for scratch hardness, which is followed by the heat treatment time (C) and the bath temperature (A).

**Table 5.** Results for ANOVA of *S/N* ratio of hardness and scratch hardness of ENB-W coating.

Microhardness					
Source	Degrees of Freedom	Adjusted Sum of Squares	Adjusted Mean of Squares	F-Value	% Contribution
A	2	0.01448	0.007239	1.05	2.78
B	2	0.22948	0.114742	16.69	44.08
C	2	0.26287	0.131437	19.12	50.49
Error	2	0.01375	0.006876		2.64
Total	8	0.52059			100.00
Scratch Hardness					
Source	Degrees of Freedom	Adjusted Sum of Squares	Adjusted Mean of Squares	F-Value	% Contribution
A	2	0.16185	0.08092	3.23	9.87
B	2	0.73544	0.36772	14.68	44.83
C	2	0.6932	0.3466	13.83	42.25
Error	2	0.05011	0.02505		3.05
Total	8	1.64059			100.00

Table 6 displays the results of the confirmation test. In comparison to the initial test run, at an optimized condition, the results reveal an improvement of 10.170% and 18.461% for hardness and scratch hardness, respectively. The experimental and predicted *S/N* ratios seem to be closely correlated with one another. A comparison of hardness values in other research works is presented in Table 7. The optimized heat-treated coatings have higher or comparable hardness with respect to other research works where ENB-W coatings were obtained from a lead-stabilized bath or stabilizer-free bath.

**Table 6.** Result of validation test of *S/N* ratio of hardness and scratch hardness of ENB-W coating.

Microhardness			
Level	Initial Parameter (A <sub>2</sub> B <sub>2</sub> C <sub>2</sub> )	Predicted Parameter (A <sub>1</sub> B <sub>3</sub> C <sub>3</sub> )	Optimal Parameter (A <sub>1</sub> B <sub>3</sub> C <sub>3</sub> )
<i>S/N</i> ratio (dB)	59.96	60.7434	60.7978
Hardness (HV <sub>100</sub> )	995	-	1096.2
Enhancement of <i>S/N</i> ratio = 1.397 dB Enhancement of hardness = 10.170%			
Scratch Hardness			
Level	Initial parameter (A <sub>2</sub> B <sub>2</sub> C <sub>2</sub> )	Predicted parameter (A <sub>1</sub> B <sub>3</sub> C <sub>3</sub> )	Optimal parameter (A <sub>1</sub> B <sub>3</sub> C <sub>3</sub> )
<i>S/N</i> ratio (dB)	21.36	22.7299	22.8353
Scratch hardness (GPa)	11.7	-	13.86
Enhancement of <i>S/N</i> ratio = 6.906 dB Enhancement of scratch hardness = 18.461%			

### 3.4. Multi-Objective Optimization

The experimental data were normalized using HB criteria as per Equation (3). Using Equation (4), GRC can be calculated. Table 8 gives the results of GRA for multi-objective optimization of hardness and scratch hardness. The lowest GRG is given an order of 9,

while the greatest GRG is given an order of 1. Using Equation (1), the  $S/N$  ratio of GRG is calculated. Further study of the  $S/N$  ratio is conducted in a manner similar to that used for single-objective optimization, and the results are given.

**Table 7.** Comparison of Vicker’s hardness obtained in present work with other research works.

B (wt.%)	W (wt.%)	Stabilizer	Heat Treatment		Hardness (HV <sub>100</sub> )	References
			Temperature (°C)	Duration (h)		
5.2–5.3 (as-deposited)	3.4 (as-deposited)	Lead nitrate	as-deposited	-	759 ± 20	8
			350	1	1181 ± 20	
			400	1	1085 ± 20	
			450	1	1067 ± 20	
3.25	1.65	Stabilizer free	as-deposited	-	645	9
1.70	2.10				690	
1.45	2.45				720	
-	-	Lead nitrate	as-deposited	-	794 ± 41	13
-	-	Lead nitrate	450	1	986 ± 44	
3.25 (as-deposited)	1.65 (as-deposited)	Stabilizer free	450	3	1096.2	Present work

**Table 8.** Results of pre-processing of data for GRA.

Exp. No.	Normalized Responses		Gray Relational Coefficients		Grade	Order	$S/N$ Ratio (dB)
	Hardness	Scratch Hardness	Hardness	Scratch Hardness			
1	0.000	0.000	0.333	0.333	0.333	9	-9.55112
2	0.442	0.297	0.473	0.416	0.444	4	-7.05234
3	1.000	1.000	1.000	1.000	1.000	1	0.00000
4	0.282	0.081	0.411	0.352	0.382	7	-8.35873
5	0.479	0.333	0.490	0.429	0.459	3	-6.76375
6	0.330	0.225	0.427	0.392	0.410	6	-7.74432
7	0.432	0.288	0.468	0.413	0.440	5	-7.13095
8	0.188	0.072	0.381	0.350	0.366	8	-8.73038
9	0.682	0.468	0.611	0.485	0.548	2	-5.22439

The total mean of  $S/N$  ratios of grade of nine experiments is shown in Table 9. According to the response table, parameter C is the most significant in determining hardness and scratch hardness. Figure S4 shows the plot of means of  $S/N$  ratios of grade. The main effect plot provides an optimal combination for maximizing hardness and scratch hardness. As a result, the  $A_1B_3C_3$  parameter combination appears to be optimal.

**Table 9.** Response table for  $S/N$  ratios of GRG.

Level	A	B	C
1	-5.534	-8.347	-8.675
2	-7.622	-7.515	-6.878
3	-7.029	-4.323	-4.632
Delta	2.088	4.024	4.043
Rank	3	2	1
Total mean $S/N$ ratio of grade = -6.728 (dB)			

The ANOVA for  $S/N$  ratios of GRG are tabulated in Table 10. It is extremely evident from the results of ANOVA that the heat treatment temperature is the most important factor in influencing the simultaneous control of both microhardness and scratch hardness for ENB-W coatings. The parameter B, i.e., heat treatment temperature, has the maximum contribution followed by C, i.e., heat treatment time and lastly by A, i.e., bath temperature in controlling the hardness and scratch hardness of an ENB-W coating.

**Table 10.** Results for ANOVA of  $S/N$  ratio of GRG.

Source	Degrees of Freedom	Adjusted Sum of Squares	Adjusted Mean of Squares	F-Value	% Contribution
A	2	6.944	3.472	1.44	10.941
B	2	27.077	13.538	5.62	42.663
C	2	24.629	12.314	5.11	38.805
Error	2	4.818	2.409		7.591
Total	8	63.467			100

The comparison of the predicted, experimental and initial condition GRG is presented in Table 11. According to Table 11, the enhancement of GRG under optimal conditions is approximately 0.658 or 192.397% compared to the initial test run. This is a substantial enhancement.

**Table 11.** Result of validation test of  $S/N$  ratio of GRG.

Parameters	Initial	Optimal Parameters	
		Prediction	Experimental
Level	$A_2B_2C_2$	$A_1B_3C_3$	$A_1B_3C_3$
Grade	0.342	0.948	1.000
Improvement of GRG = 0.658 (192.397%)			

The optical image of the constant load (10 N) scratch test of coatings at optimal parameters ( $A_1B_3C_3$ ) and the initial test condition ( $A_2B_2C_2$ ) are shown in Figure S5. The scratch width is almost uniform throughout the scratch length.

### 3.5. The Optimal ENB-W Coating Characterization

The FESEM image of ENB-W coatings at the optimal condition ( $A_1B_3C_3$ ) and initial test condition ( $A_2B_2C_2$ ) is illustrated in Figure 6. The coatings show densely packed nodulated morphology. The nodules appear slightly inflated owing to the crystallization of the coating upon heat treatment and rise in grain size. At this point, cellular boundaries start forming, as shown in Figure 6a. Again, inflation of the nodule as shown in Figure 6c at the initial test condition shows a further rise in the size of the nodules. A high magnification micrograph image of the optimal condition (Figure 6b) and initial test condition (Figure 6d) clearly shows an increase in the nodules size, indicating the occurrence of a phase transformation on heat treatment. Some micropores are also visible in the initial test condition coatings. The coatings are more compact in their optimal condition (Figure 6a) with respect to the initial test condition (Figure 6c), resulting in ploughing resistance. Furthermore, some lamellar structures are seen to be distributed on the entire surface of the coatings obtained at the optimal condition.

At the optimal condition, the heat treatment was conducted at 450 °C for 3 h. Also, coatings have a lower B content since they were developed at  $A_1$ . A detailed study of the oxidation behavior of ENB and ENB-W was undertaken by Eraslan and Ürgen [10]. There, it was revealed that in ENB coatings, there was a loss of B from the surface because of the higher diffusion mobility of B atoms compared to Ni at high temperatures. Even after 1 h heat treatment, there is a diffusion of B to the inner regions of the coating. At 450 °C, B diffuses to the surface and forms oxides of B which start evaporating, resulting in a loss of B, while at the surface, a nickel oxide layer is formed. The interdiffusion phenomenon exhibited by ENB-W coatings was also similar [10]. Thus, it is expected that the surface of coatings obtained at optimal condition may have nickel oxides with the appearance of the lamellar structures. Further analysis was therefore carried out through XRD.

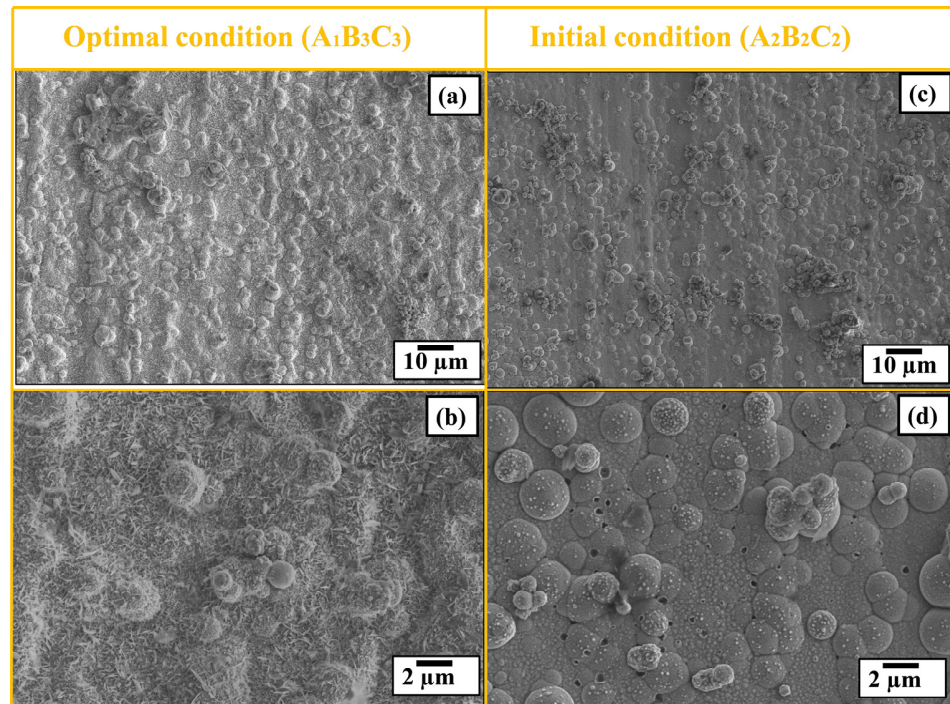


**Figure 6.** FESEM micrographs of ENB-W coatings at (a) Optimal parametric condition ( $A_1B_3C_3$ ) (b) Higher magnification image at optimal condition (c) Initial test condition ( $A_2B_2C_2$ ) and (d) Higher magnification image of initial test condition.

The XRD analyses of the ENB-W coating at an optimal parametric condition ( $A_1B_3C_3$ ) and initial test condition ( $A_2B_2C_2$ ) are depicted in Figure 7a,c, respectively, while their detailed analyses are presented in Figure 7b,d, respectively. After heat treatment, coatings crystallize and precipitate hard boride phases like  $Ni_2B$  and  $Ni_3B$ . This increases the microhardness and scratch resistance of coatings at optimized coatings. Heat treatment causes the formation of crystalline Ni (111) for  $2\theta$  at  $\sim 44^\circ$  for both the optimized and initial test condition. After heat treatment, the coating crystallization and boride precipitation is consistent with the literature [27,34]. The presence of peaks of the substrate at  $\sim 65^\circ$  is also consistent with that observed by Vitry et al. [30] for ENB coatings obtained from a stabilizer-free bath. Interestingly, oxides of iron are seen in the coating at an optimized condition, although the peak is very low for the coatings obtained at the initial condition. This supports the interdiffusion phenomenon occurring for the ENB-W coating when heat treated at  $450^\circ\text{C}$  for 3 h. The different phases, their position and FWHM are given in Table 12. Mostly, the different phases overlap. In the XRD, no oxide of Ni or W could be seen, although their presence can be captured through Raman analysis [10] and may be carried out in future research works.

**Table 12.** Different phases obtained after heat treatment of ENB-W coatings.

Combination	$2\theta$	Phase	FWHM	Crystallite Size (nm)
$A_1B_3C_3$	30.05	$Ni_3B, Fe_2O_3$	0.1600	29.712
	35.35	$Ni_3B, Fe_2O_3, Ni_2B$	0.0400	24.930
	44.17	Ni, $Ni_3B$	0.6000	20.487
	62.45	$Fe_2O_3, Ni_3B$	0.2400	14.859
	65.19	Fe	0.0800	14.299
$A_2B_2C_2$	44.49	Fe, Ni, $Ni_3B$	0.1600	20.349
	46.07	$Ni_3B, Ni_2B$	0.2000	19.687
	51.83	Ni, $Ni_2B$	0.2400	17.626
	65.01	Fe	0.2800	14.335

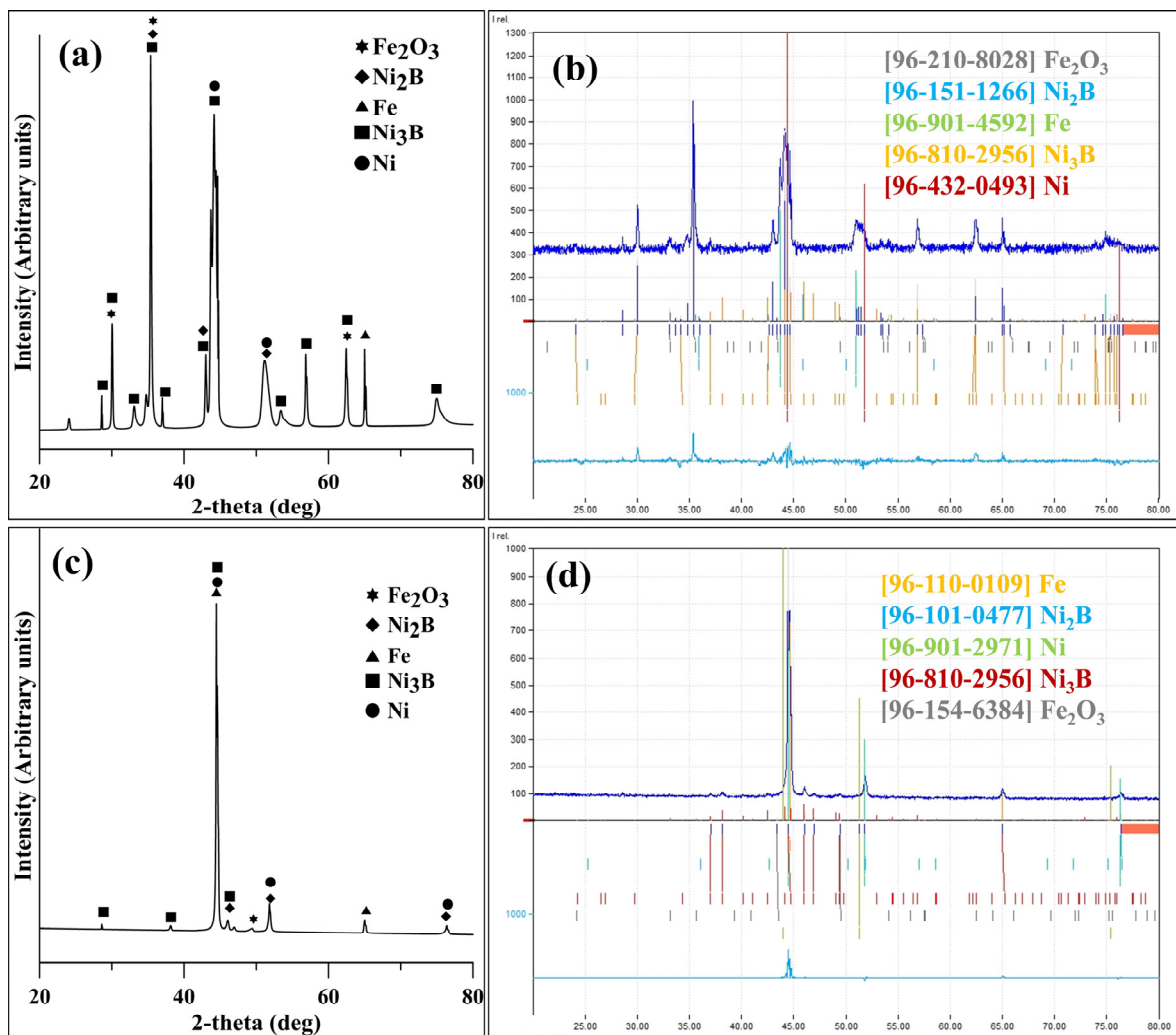


**Figure 7.** XRD analysis of ENB-W coating: (a) Optimal parametric condition ( $A_1B_3C_3$ ), (b) Detailed analysis of peaks at optimal condition (c) Initial test condition ( $A_2B_2C_2$ ) and (d) Detailed analysis of peaks at initial condition.

### 3.6. Characterizing the Adhesion and Failure of Optimized Coatings

To focus the consequence of heat treatment on the surface failure behavior of ENB-W coatings, scratch tests were conducted at a progressively increasing load. The variation of normal load with traction force, acoustics emission and coefficient of friction (COF) for the optimal condition and initial test condition are plotted in Figures 8a and 9a, respectively. The optical images of the progressive scratch test for the optimal condition and initial test condition are presented in Figures 8b and 9b, respectively. The 1st critical loads of failure for the optimized and initial test condition was found to be 8.2 N (Figure 8a) and 9 N (Figure 9a), respectively. For both conditions, 8 to 10 N is the indicated failure point. Again, this has similarity with the results of stabilizer-free as-deposited ENB-W coatings [9], where poor adherence with the substrate was seen. In another study, the COF and acoustic emission revealed that the 1st critical load of failure for an ENB coatings without stabilizer occurred at 9–13 N [18]. Also, 10–20 N was indicated in the COF and acoustic emission as the first critical load of failure for a lead tungstate-stabilized bath [37], but optical observations revealed 9.8 N [37]. The critical load for ENB coatings in a stabilizer-free bath was 20 N, whereas the critical load for ENB-Pb was 25 N as reported by Bonin et al. [19]. In another investigation by Vitry and Bonin [28], the critical load for the coating was found to be between 25 and 30 N for lead-stabilized ENB. Again, the first damage was observed at 18 to 30 N in a tin-stabilized bath [38]. Therefore, in the present work, a lower critical

load of failure was detected for heat-treated coatings through an instrumented scratch test compared to other research works.

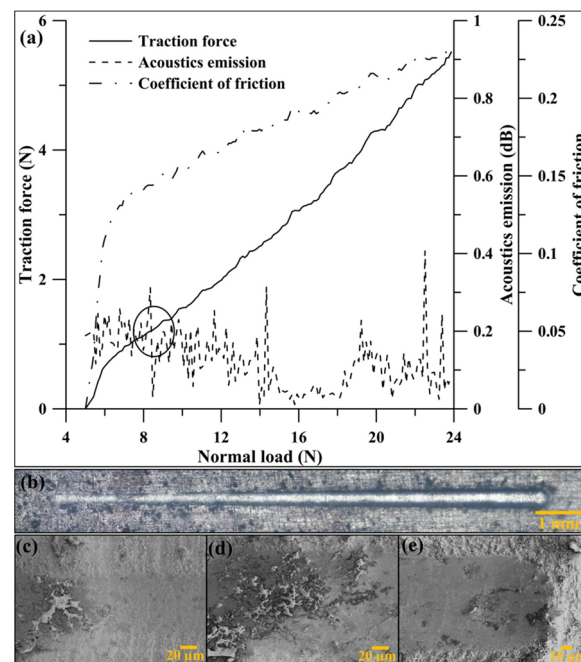


**Figure 8.** Variation of traction force, coefficient of friction and acoustic emissions are shown in (a) for progressive scratch test of coatings at optimal parametric condition ( $A_1B_3C_3$ ). Optical micrograph image of full scratch is shown in (b), while the FESEM of scratch tracks at (c) the start point, (d) region of failure indicated by (a), (e) the end point is also depicted.

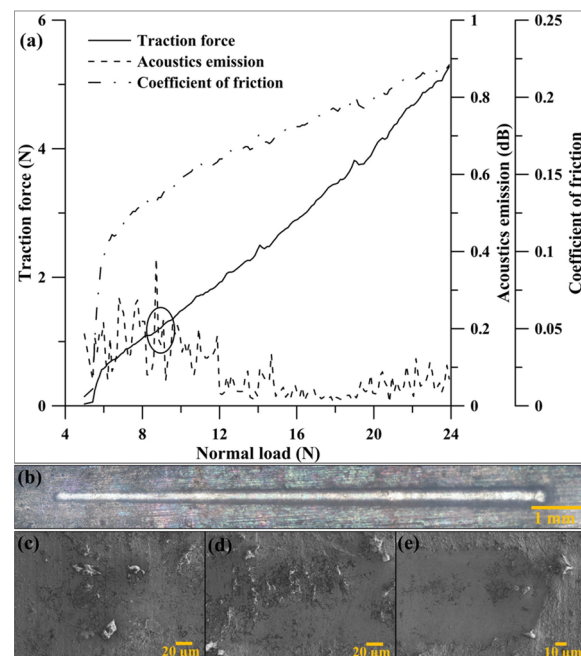


**Figure 9.** Variation of traction force, coefficient of friction and acoustic emissions are shown in (a) for progressive scratch test of coatings at initial parametric condition ( $A_2B_2C_2$ ). Optical micrograph image of full scratch is shown in (b), while the FESEM of scratch tracks at (c) the start point, (d) region of failure indicated by (a), (e) the end point is also depicted.

However, Figures 8c–e and 9c–e show the FESEM of progressive scratches at the start, failure region, and end portion for the optimal as well as initial test condition. For the optimized condition, at the initial portion of scratch, there is no crack, as shown in Figure 8c. At around 8.2 N and beyond, the plastic deformation of nodules is observable over the track, as shown in Figure 8d along with some pile up of the nodules. There is a breakage of nodule as observed in the coating failure region, as shown in Figure 8d. This may have resulted in a sudden change in the traction force and indication of first critical load of failure for optimized coatings. Finally, at the end of the scratch, there is plastic deformation. The first critical load of failure indication in Figure 8a is due to some erratic phenomenon such as the crushing of the nodules, even though no chevron or transverse cracks are seen. At the optimized condition, from the FESEM images, it is concluded that the first critical load of failure is beyond 24 N, which is significantly higher than the as-deposited stabilizer-free ENB-W deposits [9]. To some extent, this also indicates a higher adhesion of the coatings on heat treatment and a fairly ductile behavior.

At the initial parametric condition ( $A_2B_2C_2$ ) as shown in Figure 9, initially, there was no crack (Figure 9c), but at the failure region (Figure 9d), there is a crushing of the nodules as observed and some pile up of the nodules. Lastly, at the end point, there is again plastic deformation (Figure 9e). Furthermore, it is concluded that the first critical load of failure is also beyond 24 N for the coatings considered for the initial trial run. In both the cases, the coating adhesion improves especially with respect to lead-free ENB-W [9].

### 3.7. Investigations of Corrosion Resistance

The PDP-based Tafel plot of heat-treated ENB-W coatings at optimized and initial test conditions exposed to 3.5% NaCl is depicted in Figure 10. The coatings obtained at optimal condition have nobler  $E_{\text{corr}}$  compared to that at the initial condition. Table 13 compares the  $E_{\text{corr}}$  of the ENB-W coating obtained in the present work with other research works. The  $E_{\text{corr}}$  obtained in the present work is very close to that of heat-treated coatings obtained from the lead nitrate-stabilized bath. Furthermore, compared to bare AISI 1040 steel,  $E_{\text{corr}}$  is nobler for the heat-treated ENB-W coatings.

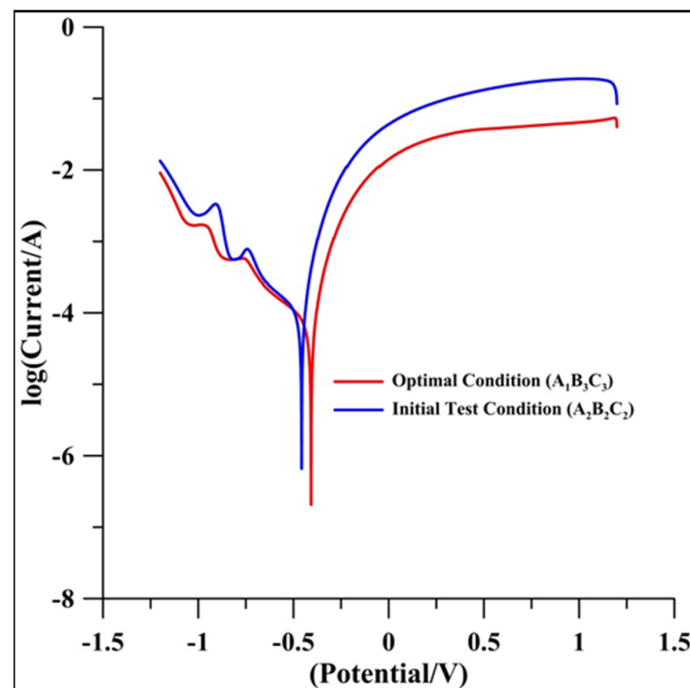


Figure 10. PDP in 3.5% NaCl solution for ENB-W coatings at optimized and initial test conditions.

The properties of ENB or ENB-W coating depend on the structure, B segregation, and grain size [27]. The nucleation of crystalline Ni is prevented by higher B segregation and

results in an amorphous structure of ENB coatings. The amorphous ENB coatings have higher corrosion resistance than crystalline coatings. Post-crystallization, grain growth takes place and nodular boundaries are clearly observed on the surface of ENB coatings, which form active sites of corrosion. In fact, a nanocrystalline ENB coating [39] where the coating lies in the low-B range shows poor corrosion resistance. In the present work, the corrosion resistance of heat-treated, crystalline ENB-W coating is enhanced. Yildiz et al. [6] studied the PDP of an ENB-W coating and came to the conclusion that the better corrosion resistance of ENB-W coatings after heat treatment is caused by W diffusion to the surface through grain boundaries. This tends to inhibit the corrosion of ENB-W coatings. Similar results were also detected by Mukhopadhyay et al. [40]. In the present work, a similar mechanism is expected to inhibit the corrosion of coatings. Furthermore, optimized heat-treated coatings surface show a distribution of lamellar structures, which may be due to oxide products formed as a result of heat treatment or the suggested interdiffusion phenomenon, which requires further investigation. This may have some effect on corrosion protection.

**Table 13.** PDP results of ENB-W coatings at optimized and initial test conditions.

Sl. No.	Coating	Coatings Bath	$E_{corr}$ (mV)	Reference
1	ENB-W (Optimal condition)	Stabilizer free	−407	Present case
2	ENB-W (Initial test condition)		−457	
3	ENB-W (350 °C for 1 h)	Lead nitrate	−392	40
4	ENB-W (450 °C for 1 h)	stabilized	−453	40
5	AISI 1040 steel	-	−710	9

The FESEM micrograph of the corroded part of ENB-W coatings for the optimized ( $A_1B_3C_3$ ) and initial test conditions ( $A_2B_2C_2$ ) is shown in Figure 11. Some broken nodules may be observed at the optimal condition of ENB-W coatings (Figure 11a), and a spongy appearance is observed. The structures appear to be more lamellar type [24] in the higher magnification image in Figure 11b [24]. Several cracks appear at the initial test condition as shown in Figure 11c. A higher magnification image (Figure 11d) displays lamellar structures with aggregates of nodules. Due to this, a slight deterioration in corrosion resistance is seen for the coatings obtained at the optimal condition. The corrosion products tend to slow down the electrolyte penetration and corrosive attack, which may lead to an increase in corrosion resistance [41]. León et al. [42] found a rise in the corrosion resistance of ENP and ENP- $Al_2O_3$  coatings when heat treated above 400 °C. León et al. [42] suggested that an enhanced EN coating adherence to substrates and formation of stable intermetallic compounds after heat treatment could enhance the corrosion resistance. In the present case, it was seen from the scratch tests that the adhesion of coatings improves, and the first critical load of failure is delayed on heat treatment. This may also promote the corrosion resistance of heat-treated ENB-W coatings.

A further analysis of the corrosion was carried out through the EDS mapping and shown in Figure 12. The elemental distribution was seen, which would provide further insights. The presence and distribution of B, O, Fe, Ni and W for optimized as well as initial test conditions is denoted by different color, as depicted in Figure 12a,b, respectively. The intensity of Ni in the optimized condition is higher with respect to the initial test condition, and hence, it is concluded that the corrosion products are nickel rich or oxides of nickel. Some distribution of Fe and its oxide (seen in XRD, Figure 7a) is also confirmed in the EDS map in Figure 12a. The intensity of Fe in the initial condition is higher in Figure 12b. Thus, the corrosive products formed at the optimized condition are nickel rich and lead to enhanced corrosion resistance. Whereas, due to chloride attack, there may have been some coating breakage and entry of corrosive media to the substrate.

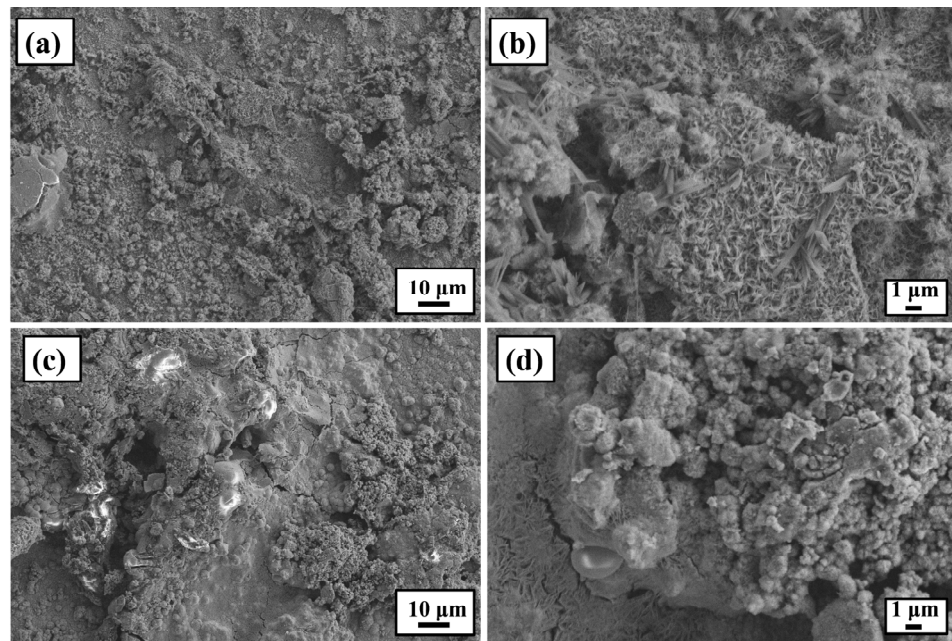


**Figure 11.** FESEM micrograph of corroded region of ENB-W coatings for (a) optimized condition ( $A_1B_3C_3$ ), (b) higher magnification of optimized condition, (c) initial test condition ( $A_2B_2C_2$ ) and (d) higher magnification of initial test condition.

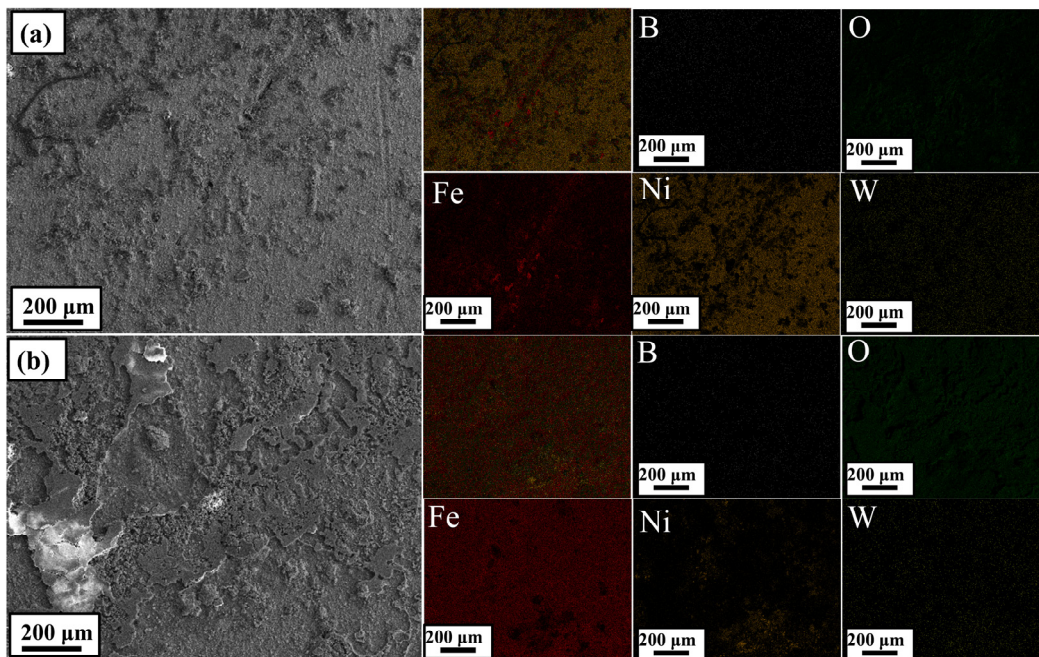


**Figure 12.** EDS mapping of corroded region of ENB-W coatings for (a) optimized ( $A_1B_3C_3$ ) and (b) initial test conditions ( $A_2B_2C_2$ ).

#### 4. Conclusions

The optimization of mechanical properties, namely surface microhardness and scratch hardness, was carried out in the present work for ENB-W coatings deposited from a stabilizer-free bath. To achieve ENB-W coatings with varying W and B, the bath temperature was varied. The heat treatment temperature and duration were varied to achieve various degrees of crystallization in coating. Finally, coating failure was determined, and the corrosion resistance of optimized coatings was examined. A Taguchi-based experimental

design was followed, and L<sub>9</sub> OA was chosen to carry out the experiments. The main outcomes are as follows:

- A typical nodular morphology was observed in the as-deposited coatings. XRD results revealed a typical mixed amorphous nanocrystalline nature with overlapping peaks of Fe and Ni.
- The optimal predicted hardness and scratched hardness values were 1096.2 HV<sub>100</sub> and 13.86 GPa, respectively, at a parametric combination of A<sub>1</sub>B<sub>3</sub>C<sub>3</sub>.
- The heat treatment temperature had the highest influencing effect when the surface microhardness and scratch hardness were considered simultaneously.
- The characterization of coatings at optimal condition revealed the formation of lamellar structures dispersed over the entire surface. This is expected to be oxides of nickel. Furthermore, oxides of iron were also seen in XRD. This indicates a possible interdiffusion phenomenon and requires further investigation.
- The failure of the coatings within 5–24 N was investigated using a progressive scratch test. Investigation of the scratch tracks revealed no cracks and possibly higher adhesion of the coatings due to heat treatment. Overall, ductile behavior was seen, and the first critical load of failure improved compared to ENB-W coatings obtained from a stabilizer-free bath.
- Finally, the electrochemical corrosion behavior was investigated for the optimized coatings. Heat-treated coatings showed an E<sub>corr</sub> of −407 mV which was superior compared to the substrate.

**Supplementary Materials:** The following supporting information can be downloaded at: <https://www.mdpi.com/article/10.3390/coatings13091585/s1>, Figure S1: Contour plots of surface microhardness with variation of (a) heat treatment temperature vs. bath temperature (b) heat treatment time vs. heat treatment temperature and (c) heat treatment time vs. bath temperature.; Figure S2: Contour plots of scratch hardness with variation of (a) heat treatment temperature vs. bath temperature (b) heat treatment time vs. heat treatment temperature and (c) heat treatment time vs. bath temperature; Figure S3: Main effect plot of S/N ratio for (a) hardness and (b) scratch hardness; Figure S4: Plot of means of S/N ratio of grade; Figure S5: Constant load scratch test of coatings at (a) optimal parameters (A<sub>1</sub>B<sub>3</sub>C<sub>3</sub>), (b) initial test condition (A<sub>2</sub>B<sub>2</sub>C<sub>2</sub>).

**Author Contributions:** Conceptualization, R.A., O.P., L.S.B. and A.M.; Data curation, R.A.; Formal analysis, R.A.; Funding acquisition, O.P., L.S.B. and A.M.; Investigation, R.A.; Methodology, R.A. and A.M.; Project administration, O.P., L.S.B. and A.M.; Resources, A.M.; Software, R.A. and A.M.; Supervision, O.P., L.S.B. and A.M.; Visualization, O.P., L.S.B. and A.M.; Writing—original draft, R.A.; Writing—review and editing, O.P., L.S.B. and A.M. All authors have read and agreed to the published version of the manuscript.

**Funding:** This research received no external funding.

**Institutional Review Board Statement:** Not applicable.

**Informed Consent Statement:** Not applicable.

**Data Availability Statement:** The data presented in this study are available in the article.

**Acknowledgments:** The authors gratefully acknowledge the Central Instrumentation Facility and the funding provided by Institute Seed Money Scheme—2020 (Ref. No.: GO/Estb/SMS/2020-21/2262) of Birla Institute of Technology, Mesra, Ranchi—835215.

**Conflicts of Interest:** The authors declare no conflict of interest. The funders had no role in the design of the study; in the collection, analyses, or interpretation of data; in the writing of the manuscript; or in the decision to publish the results.

## Abbreviations

EN	Electroless nickel
ENP	Electroless Ni-P
ENB	Electroless nickel boron

ENB-W	Electroless Ni-B-W
GRA	Grey relational analysis
ANOVA	Analysis of variance
FESEM	Field emission scanning electron microscope
OA	Orthogonal array
XRD	X-ray diffraction
A <sub>1</sub>	85 °C coating bath temperature
A <sub>2</sub>	90 °C coating bath temperature
A <sub>3</sub>	95 °C coating bath temperature
B <sub>1</sub>	350 °C Heat treatment temperature
B <sub>2</sub>	400 °C Heat treatment temperature
B <sub>3</sub>	450 °C Heat treatment temperature
C <sub>1</sub>	1 h Heat treatment duration
C <sub>2</sub>	2 h Heat treatment duration
C <sub>3</sub>	3 h Heat treatment duration
PDP	Potentiodynamic polarization
HB	Higher-the-better
S/N ratios	Signal-to-noise ratios
GRG	Gray relational grade
GRC	Gray relational coefficients
FWHM	Full width at half maximum
COF	Coefficient of friction

## References

- Vitry, V.; Hastir, J.; Mégret, A.; Yazdani, S.; Yunacti, M.; Bonin, L. Recent advances in electroless nickel-boron coatings. *Surf. Coat. Technol.* **2022**, *429*, 127937. [[CrossRef](#)]
- Sahoo, P.; Das, S.K. Tribology of Electroless Nickel Coatings—A Review. *Mater. Des.* **2011**, *32*, 1760–1775. [[CrossRef](#)]
- Sudagar, J.; Lian, J.; Sha, W. Electroless Nickel, Alloy, Composite and Nano Coatings—A Critical Review. *J. Alloys Compd.* **2013**, *571*, 183–204. [[CrossRef](#)]
- Aydeniz, A.I.; Göksenli, A.; Dil, G.; Muhaffel, F.; Calli, C.; Yüksel, B. Electroless Ni-B-W Coatings for Improving Hardness, Wear and Corrosion Resistance. *Mater. Technol.* **2013**, *47*, 803–806.
- Mukhopadhyay, A.; Barman, T.K.; Sahoo, P. Wear and Friction Characteristics of Electroless Ni-B-W Coatings at Different Operating Temperatures. *Mater. Res. Express* **2018**, *5*, 026526. [[CrossRef](#)]
- Yildiz, R.A.; Göksenli, A.; Yüksel, B.H.; Muhaffel, F.; Aydeniz, A. Effect of Annealing Temperature on the Corrosion Resistance of Electroless Produced Ni-B-W Coatings. *Adv. Mater. Res.* **2013**, *651*, 263–268. [[CrossRef](#)]
- Drovosekov, A.B.; Ivanov, M.V.; Krutskikh, V.M.; Lubnin, E.N.; Polukarov, Y.M. Chemically Deposited Ni-W-B Coatings: Composition, Structure, and Properties. *Prot. Met.* **2005**, *41*, 55–62. [[CrossRef](#)]
- Mukhopadhyay, A.; Barman, T.K.; Barman, P. Tribological Behavior of Electroless Ni-B-W Coating at Room and Elevated Temperatures. *Proc. Inst. Mech. Eng. Part J J. Eng. Tribol.* **2018**, *232*, 1450–1466. [[CrossRef](#)]
- Agrawal, R.; Mukhopadhyay, A. Inclusion of W in electroless Ni-B coating developed from a stabilizer free bath and investigation of its tribological behaviour. *J. Indian Chem. Soc.* **2023**, *100*, 100966. [[CrossRef](#)]
- Eraslan, S.; Ürgen, M. Oxidation Behavior of Electroless Ni-P, Ni-B and Ni-W-B Coatings Deposited on Steel Substrates. *Surf. Coat. Technol.* **2015**, *265*, 46–52. [[CrossRef](#)]
- Barman, M.; Barman, T.K.; Sahoo, P. Tribo-Mechanical Characterisation of Borohydride Reduced Ni-B-W Coatings. *J. Inst. Eng. (India) Ser. D* **2023**, *1–21*. [[CrossRef](#)]
- Mukhopadhyay, A.; Barman, T.K.; Sahoo, P. Investigation of Tribological Performance of Electroless Ni-B-W Coatings At High Temperature and Its Optimization. In *Optimization Methods for Engineering Problems*; CRC Press: Boca Raton, FL, USA, 2023; p. 239.
- Nemane, V.; Sharma, V.; Chatterjee, S. Tribological Electroless Ternary Ni-B-W Coatings: A Suitable Alternative to Hard Chromium Coatings. *J. Tribol.* **2022**, *144*, 121401. [[CrossRef](#)]
- Nemane, V.; Chatterjee, S. Nanomechanical, Tribological, and Scratch Properties of Electroless Ni-B-W Alloy and Ni-B-W-SiC Composite Coatings. *J. Tribol.* **2022**, *144*, 051402. [[CrossRef](#)]
- Nemane, V.; Chatterjee, S. Scratch and Sliding Wear Testing of Electroless Ni-B-W Coating. *ASME J. Tribol.* **2020**, *142*, 021705. [[CrossRef](#)]
- Zhao, F.; Hu, H.; Yu, J.; Lai, J.; He, H.; Zhang, Y.; Wang, D. Mechanical and Tribological Properties of Ni-B and Ni-BW Coatings Prepared by Electroless Plating. *Lubricants* **2023**, *11*, 42. [[CrossRef](#)]
- Nemane, V.; Chatterjee, S. Evaluation of microstructural, mechanical, and tribological characteristics of Ni-B-W-SiC electroless composite coatings involving multi-pass scratch test. *Mater. Charact.* **2021**, *180*, 111414. [[CrossRef](#)]
- Agrawal, R.; Mukhopadhyay, A. Development of Ni-B electroless coating from stabilizer free bath and characterization of high temperature tribological behaviour, scratch and corrosion resistance. *Surf. Topogr. Metrol. Prop.* **2022**, *10*, 045028. [[CrossRef](#)]

19. Bonin, L.; Castro, C.C.; Vitry, V.; Hantson, A.L.; Delaunois, F. Optimization of electroless Ni-B deposition without stabilizer, based on surface roughness and plating rate. *J. Alloys Compd.* **2018**, *767*, 276–284. [[CrossRef](#)]
20. Yunacti, M.; Mégret, A.; Staia, M.H.; Montagne, A.; Vitry, V. Characterization of electroless nickel–boron deposit from optimized stabilizer-free bath. *Coatings* **2021**, *11*, 576. [[CrossRef](#)]
21. Taguchi, G. *Introduction to Quality Engineering*; Asian Productivity Organization: Tokyo, Japan, 1990.
22. Deng, J. Introduction to grey system. *J. Grey. Syst.* **1989**, *1*, 1–24.
23. Das, S.K.; Sahoo, P. Tribological characteristics of electroless Ni–B coating and optimization of coating parameters using Taguchi based grey relational analysis. *Mater. Des.* **2011**, *32*, 2228–2238. [[CrossRef](#)]
24. Onder, O.C.; Yilgor, E.; Yilgor, I. Critical parameters controlling the properties of monolithic poly (lactic acid) foams prepared by thermally induced phase separation. *J. Polym. Sci. Part B Polym. Phys.* **2019**, *5*, 98–108. [[CrossRef](#)]
25. Barman, M.; Barman, T.K.; Sahoo, P. Tribo-mechanical characterization of ENB alloy coatings: Effect of heat-treatment temperature and sodium borohydride concentration. *Facta Univ.* **2022**. [[CrossRef](#)]
26. Barman, M.; Barman, T.K.; Sahoo, P. Effect of heat-treatment temperature and borohydride concentration on corrosion behaviour of ENB coating. *Proc. Inst. Mech. Eng Part C* **2023**, *237*, 183–200. [[CrossRef](#)]
27. Krishnaveni, K.; Narayanan, T.S.; Seshadri, S.K. Electroless Ni–B coatings: Preparation and evaluation of hardness and wear resistance. *Surf. Coat. Technol.* **2005**, *190*, 115–121. [[CrossRef](#)]
28. Vitry, V.; Bonin, L. Increase of boron content in electroless nickel–boron coating by modification of plating conditions. *Surf. Coat. Technol.* **2017**, *311*, 164–171. [[CrossRef](#)]
29. Vitry, V.; Kanta, A.F.; Dille, J.; Delaunois, F. Structural state of electroless nickel–boron deposits (5 wt.% B): Characterization by XRD and TEM. *Surf. Coat. Technol.* **2012**, *206*, 3444–3449. [[CrossRef](#)]
30. Vitry, V.; Yunacti, M.; Mégret, A.; Khalid, H.A.; Staia, M.H.; Montagne, A. Selection of New Heat Treatment Conditions for Novel Electroless Nickel–Boron Deposits and Characterization of Heat-Treated Coatings. *Coatings* **2022**, *13*, 1. [[CrossRef](#)]
31. Bülbül, F.; Altun, H.; Ezirmik, V.; Küçük, Ö. Investigation of structural, tribological and corrosion properties of electroless Ni–B coating deposited on 316L stainless steel. *Proc. Inst. Mech. Eng. Part J* **2013**, *227*, 629–639. [[CrossRef](#)]
32. Çelik, İ.; Karakan, M.; Bülbül, F. Investigation of structural and tribological properties of electroless Ni–B coated pure titanium. *Proc. Inst. Mech. Eng. Part J* **2016**, *230*, 57–63. [[CrossRef](#)]
33. Hamid, Z.A.; Hassan, H.B.; Attyia, A.M. Influence of deposition temperature and heat treatment on the performance of electroless Ni–B films. *Surf. Coat. Technol.* **2010**, *205*, 2348–2354. [[CrossRef](#)]
34. Pal, S.; Verma, N.; Jayaram, V.; Biswas, S.K.; Riddle, Y. Characterization of phase transformation behaviour and microstructural development of electroless Ni–B coating. *J. Mater. Sci. Eng. A* **2011**, *528*, 8269–8276. [[CrossRef](#)]
35. Balaraju, J.N.; Priyadarshi, A.; Kumar, V.; Manikandanath, N.T.; Kumar, P.P.; Ravisankar, B. Hardness and wear behaviour of electroless Ni–B coatings. *Mater. Sci. Technol.* **2016**, *32*, 1654–1665. [[CrossRef](#)]
36. Correa, E.; Zuleta, A.A.; Guerra, L.; Gómez, M.A.; Castaño, J.G.; Echeverría, F.; Thompson, G.E. Tribological behavior of electroless Ni–B coatings on magnesium and AZ91D alloy. *Wear* **2013**, *305*, 115–123. [[CrossRef](#)]
37. Vitry, V.; Kanta, A.F.; Delaunois, F. Mechanical and wear characterization of electroless nickel–boron coatings. *Surf. Coat. Technol.* **2011**, *206*, 1879–1885. [[CrossRef](#)]
38. Bonin, L.; Vitry, V.; Delaunois, F. The tin stabilization effect on the microstructure, corrosion and wear resistance of electroless Ni–B coatings. *Surf. Coat. Technol.* **2019**, *357*, 353–363. [[CrossRef](#)]
39. Baskaran, I.; Sankara Narayanan, T.S.N.; Stephen, A. Corrosion resistance of electroless Ni–low B coatings. *Trans. IMF* **2009**, *87*, 221–224. [[CrossRef](#)]
40. Mukhopadhyay, A.; Barman, T.K.; Sahoo, P. Tribological behavior and corrosion resistance of electroless Ni–B–W coatings. *J. Mol. Eng. Mater.* **2017**, *5*, 1750010. [[CrossRef](#)]
41. Mukhopadhyay, A.; Barman, T.K.; Sahoo, P. Effect of heat treatment on microstructure and corrosion resistance of Ni–B–W–Mo coating deposited by electroless method. *Surf. Rev. Lett.* **2018**, *25*, 1950023. [[CrossRef](#)]
42. León, C.; García-Ochoa, E.; García-Guerra, J.; González-Sánchez, J. Annealing temperature effect on the corrosion parameters of autocatalytically produced Ni–P and Ni–P–Al<sub>2</sub>O<sub>3</sub> coatings in artificial seawater. *Surf. Coat. Technol.* **2010**, *205*, 2425–2431. [[CrossRef](#)]

**Disclaimer/Publisher’s Note:** The statements, opinions and data contained in all publications are solely those of the individual author(s) and contributor(s) and not of MDPI and/or the editor(s). MDPI and/or the editor(s) disclaim responsibility for any injury to people or property resulting from any ideas, methods, instructions or products referred to in the content.